Geophysical Research Letters

Supporting Information for

Emergent Constraints on Future Projections of Tibetan Plateau Warming in Winter

Shuzhen Hu[1], Lu Wang[1]*, Xiaolong Chen[2], Tianjun Zhou[2,3], and Pang-Chi Hsu[1]*

[1]Key Laboratory of Meteorological Disaster, Ministry of Education (KLME) / Joint International Research Laboratory of Climate and Environmental Change (ILCEC) / Collaborative Innovation Center on Forecast and Evaluation of Meteorological Disasters (CIC-FEMD), Nanjing University of Information Science and Technology, Nanjing, China.
[2]State Key Laboratory of Numerical Modeling for Atmospheric Sciences and Geophysical Fluid Dynamics, Institute of Atmospheric Physics, Chinese Academy of Sciences, Beijing, China.
[3]College of Earth and Planetary Sciences, The University of Chinese Academy of Sciences, Beijing, China.

Contents of this file

Introduction

The supporting information describes the calculation of the feedback parameter (see Text S1) and the Leave-one-out perfect model test (see Text S2) in detail. In addition, the information about the 28 CMIP6 models used in this study (see Table S1), variables required for local energy budget diagnosis (see Table S2), and five sets of radiative kernels (see Table S3) are also listed.

Text S1. The calculation of the feedback parameter

Following Soden et al. (2008), the feedback parameter is calculated with the following form:

$$\lambda_i = K_i \frac{\Delta X_i}{\Delta T_{2m}}. \quad (S1)$$

K_i represents the 'radiative kernel', which has been developed by various research groups and can be downloaded directly. ($\frac{\Delta X_i}{\Delta T_{2m}}$) denotes the 'climate response pattern', defined as the ratio of the climatology change (Δ) in a given variable X_i and T_{2m} between two periods. The first four feedback parameters (λ_i with i = 0 to 3) are calculated directly by Equation S1, while the cloud feedback parameter (λ_4) is computed as the residual for balancing all the other terms in the local energy budget diagnostic (Equation S2), due to the existence of strong nonlinearity in cloud feedback.

$$\lambda_4 = -\frac{(F + \lambda_0 \Delta T_{2m} + \lambda_1 \Delta T_{2m} + \lambda_2 \Delta T_{2m} + \lambda_3 \Delta T_{2m} + \Delta SHF + \Delta AHT)}{\Delta T_{2m}}. \quad (S2)$$

Note that in this study we have used five sets of radiative kernel data (Table S3) to calculate the feedback parameters to reduce the result dependence. The right-hand side terms of Equation 1 are calculated using each radiative kernel data first, and then obtained the average.

Text S2. Leave-one-out perfect model test

Following previous studies (Brunner et al., 2020; Chen et al., 2023; Hersbach, 2000), we apply a leave-one-out perfect model test to evaluate the skill of the two-step constraint method developed in this study. The brief descriptions are given below:

1) Among the 28 CMIP6 models in use, we select model i as a target model, and take its historical simulated result as pseudo-observation and its future projection as pseudo-warming.

2) The projected warming of the remaining 27 models is then constrained by our two-step constraint method, calibrated by the pseudo-observation.

3) We repeat the steps above for all models in the ensemble.

4) Two statistics, mean-square error (MSE) and the other is continuous ranked probability skill score (CRPSS), are used to measure the quality of the constrained projection, following previous studies (Brunner et al., 2020; Chen et al. 2023; Hersbach, 2000). The MSE is defined as:

$$MSE = \frac{1}{n}\sum_{i=1}^{n}\left(\overline{Y_{C_i}} - Y_{PSE_i}\right)^2, \quad (S3)$$

where $\overline{Y_{C_i}}$ denotes the constrained expectation of future total TP warming, Y_{PSE_i} denotes the future total TP warming projected by model i. The CRPSS is defined as:

$$CRPSS = \frac{1}{n}\sum_{i=1}^{n}\left\{\int_{-\infty}^{\infty}\left[P_{C_i}(Y) - P_{PSE_i}(Y)\right]^2 dY\right\}, \quad (S4)$$

where $P_{C_i}(Y)$ denotes the cumulative distributions of constrained future total TP warming, $P_{PSE_i}(Y)$ denotes the cumulative distributions of future total TP warming projected by model i.

MSE and CRPSS are calculated between the constrained projection and pseudo warming, as well as between the unconstrained projection and pseudo warming. Lower MSE and CRPSS values for the constrained projection relative to the unconstrained projection suggest an improvement of the constrained projection compared to the unconstrained projection, indicating high-quality constrained projections.

Table S1. List of the 28 CMIP6 models used in this study, all of which provide the 19 variables shown in Table S2. The availability of the variable snow cover (snc; units: %) is listed in the rightmost column.

Model number	Model name	Institution (country)	Resolution (latitude grid × longitude grid)	Additional variables
1	BCC-CSM2-MR	BCC (China)	160 × 320	snc
2	CESM2-WACCM	NCAR (USA)	192 × 288	snc
3	CMCC-CM2-SR5	CMCC (Italy)	192 × 288	snc
4	FGOALS-f3-L	CAS (China)	180 × 288	snc
5	GFDL-ESM4	NOAA-GFDL (USA)	180 × 288	–
6	IPSL-CM6A-LR	IPSL (France)	143 × 144	snc
7	MIROC6	MIROC (Japan)	128 × 256	snc
8	MPI-ESM1-2-HR	MPI-M (Germany)	192 × 384	snc
9	MPI-ESM1-2-LR	MPI-M (Germany)	96 × 192	snc
10	MRI-ESM2-0	MRI (Japan)	160 × 320	snc
11	NESM3	NUIST (China)	96 × 192	–
12	AWI-CM-1-1-MR	AWI (Germany)	192 × 384	–
13	CAS-ESM2-0	CAS (China)	128 × 256	snc
14	CIESM	THU (China)	192 × 288	snc
15	CMCC-ESM2	CMCC (Italy)	192 × 288	snc
16	FGOALS-g3	CAS (China)	80 × 180	snc
17	INM-CM4-8	INM (Russia)	120 × 180	–
18	INM-CM5-0	INM (Russia)	120 × 180	–
19	EC-Earth3	EC-Earth-Cons (Europe)	256 × 512	snc
20	EC-Earth3-Veg	EC-Earth-Cons (Europe)	256 × 512	snc
21	ACCESS-CM2	CSIRO-ARCCSS (Australia)	144 × 192	–
22	CanESM5	CCCMA (Canada)	64 × 128	snc
23	CanESM5-1	CCCMA (Canada)	64 × 128	snc
24	KACE-1-0-G	NIMS-KMA (Korea)	144 × 192	–
25	ACCESS-ESM1-5	CSIRO-ARCCSS (Australia)	144 × 192	–
26	EC-Earth3-CC	EC-Earth-Cons (Europe)	256 × 512	snc
27	EC-Earth3-Veg-LR	EC-Earth-Cons (Europe)	160 × 320	snc
28	IITM-ESM	CCCR-IITM (India)	94 × 192	–

Table S2. Variables required for local energy budget diagnosis.

Attribute name	Unit
2m temperature	K
Surface temperature	K
Air temperature	K
Specific humidity	$g\ g^{-1}$
Surface pressure	Pa
Surface sensible heat flux	$W\ m^{-2}$
Surface latent heat flux	$W\ m^{-2}$
Surface upwelling longwave radiation	$W\ m^{-2}$
Surface downwelling longwave radiation	$W\ m^{-2}$
Surface downwelling clear-sky longwave radiation	$W\ m^{-2}$
Surface upwelling shortwave radiation	$W\ m^{-2}$
Surface upwelling clear-sky shortwave radiation	$W\ m^{-2}$
Surface downwelling shortwave radiation	$W\ m^{-2}$
Surface downwelling clear-sky shortwave radiation	$W\ m^{-2}$
TOA outgoing longwave radiation	$W\ m^{-2}$
TOA outgoing clear-sky longwave radiation	$W\ m^{-2}$
TOA outgoing shortwave radiation	$W\ m^{-2}$
TOA outgoing clear-sky shortwave radiation	$W\ m^{-2}$
TOA incident shortwave radiation	$W\ m^{-2}$

Table S3. Information about the radiative kernels used in this study.

Source of radiative kernel	Base climate	Off-line radiative transfer model/code	Horizontal resolution (°)
CloudSat (Kramer et al., 2019)	2B-FLXHR-LIDAR dataset for 2009, except for March and December, which were replaced with data from 2008	2B-FLXHR-LIDAR R05	2 × 2.5
RRTM_ERAI (Huang et al., 2017)	ERAI reanalysis dataset for 2008–2012	RRTM	2.5 × 2.5
HadGEM3-GA7.1 (Smith et al., 2020)	One-year integration of the GCM forced by the pre-industrial state	SOCRATES	1.25 × 1.875
CESM-CAM5 (Pendergrass et al., 2018)	Data for the first member of CESM Version 1.1.2 for 2006	PORT	0.94 × 1.25
CAM3 (Shell et al., 2008)	CAM3 control run data for 2006	CAM3	2.8 × 2.8

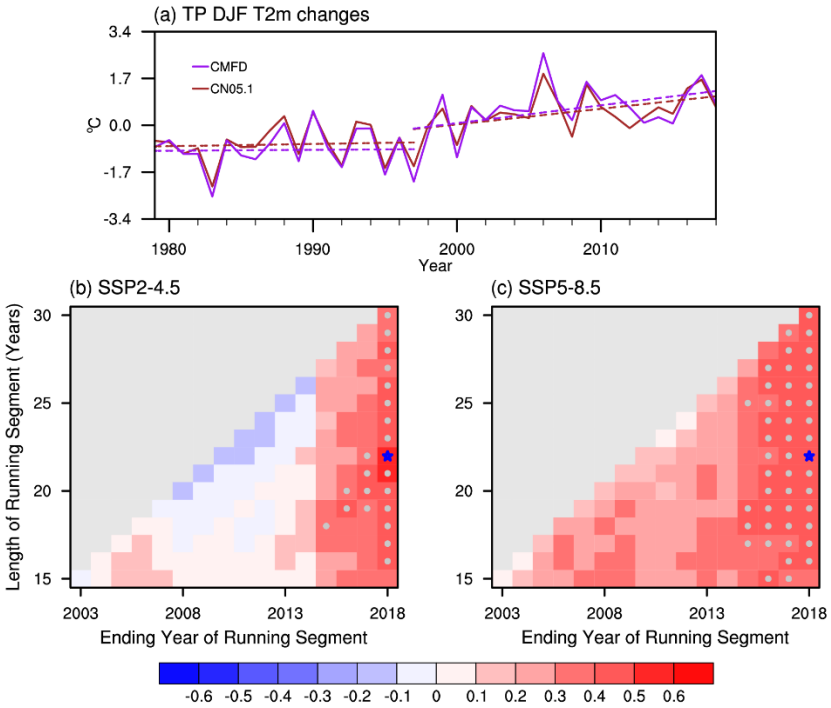

Figure S1. (a) Temporal evolutions (solid line) of winter T_{2m} changes (units: ℃) over the TP relative to the average of 1985–2014, based on observational results derived from CN05.1 (brown) and CMFD (purple), respectively. The dashed lines show the linear trend of T_{2m} during 1979–1997 and 1997–2020, respectively. (b) Inter-model correlations between the simulated TP temperature changes over different historical periods relative to a fixed climatology (1985–2014) and the projected change in Albedo-induced temperature in the future period (2071–2100) across 28 CMIP6 models under the SSP2-4.5 scenario. Gray dots denote that the correlation coefficient is statistically significant at the 95% confidence level based on the Student's t-test. The highest correlation coefficient is marked by a blue star. (c) As in (b), but for the SSP5-8.5 scenario.

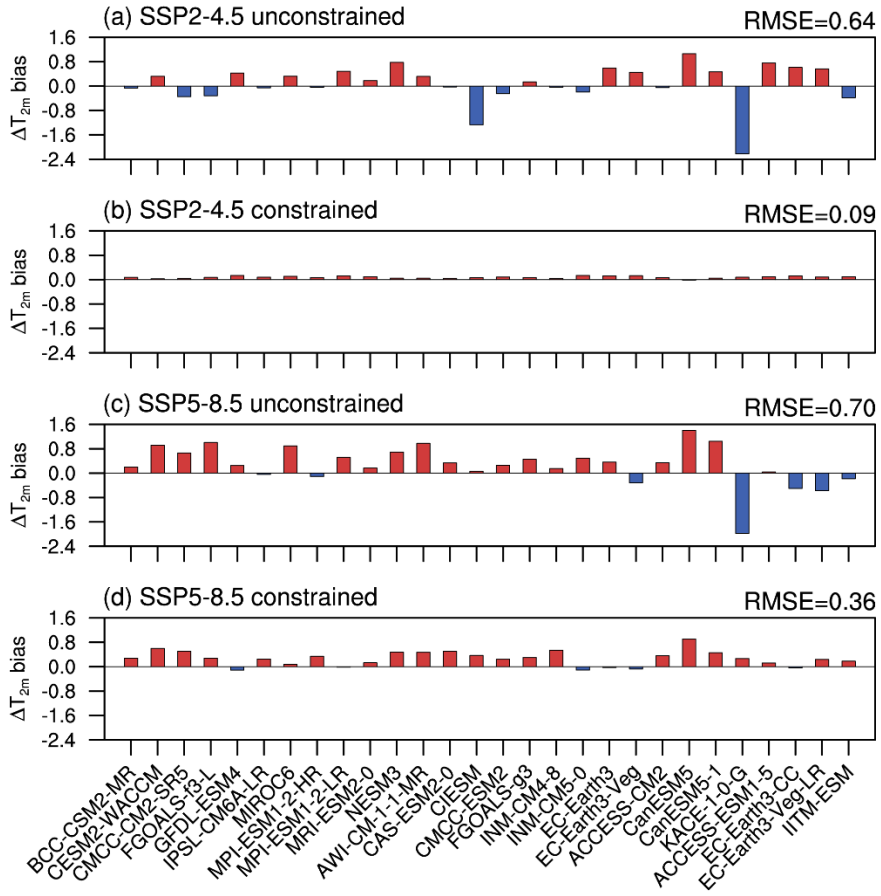

Figure S2. The bias of (a) unconstrained and (b) constrained TP temperature changes (2015–2022 minus 1985–2014) for each model under the SSP2-4.5 scenario, compared with the observational result derived from CN05.1. The root-mean-square error (RMSE) of the biases is given in the upper-right corner of each panel. (c–d) as in (a–b), but for the results under the SSP5-8.5 scenario.

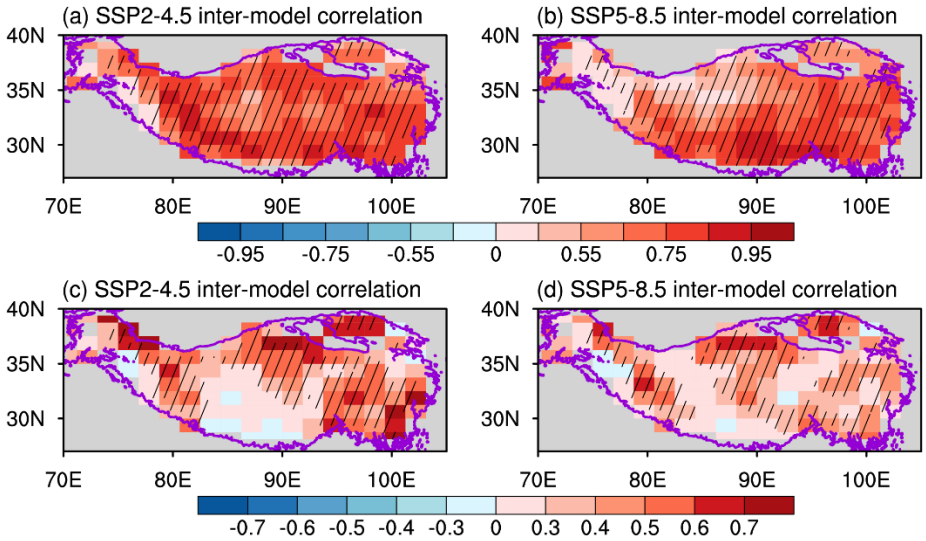

Figure S3. Spatial distribution of inter-model correlation between future total temperature change and that induced by Albedo in winter under the (a) SSP2-4.5 and (b) SSP5-8.5 scenarios, respectively. The areas with diagonal slashes indicate that the correlation coefficient is statistically significant at the 95% confidence level based on the Student's t-test. (c–d) As in (a–b), but for the inter-model correlation between future Albedo-induced temperature change and historical temperature change in winter.

References

Brunner, L., Pendergrass, A. G., Lehner, F., Merrifield, A. L., Lorenz, R., & Knutti, R. (2020). Reduced global warming from CMIP6 projections when weighting models by performance and independence. *Earth System Dynamics*, *11*, 995–1012. https://doi.org/10.5194/esd-11-995-2020

Chen, Z., Zhou, T., Chen, X., Zhang, W., Zuo, M., Man, W., & Qian, Y. (2023). Emergent constrained projections of mean and extreme warming in China. *Geophysical Research Letters*, *50*, e2022GL102124. https://doi.org/10.1029/2022GL102124

Hersbach, H. (2000). Decomposition of the continuous ranked probability score for ensemble prediction systems. *Weather and Forecasting*, *15*(5), 559–570. https://doi.org/10.1175/1520-0434(2000)015<0559:DOTCRP>2.0.CO;2

Huang, Y., Xia, Y., & Tan, X. (2017). On the pattern of CO_2 radiative forcing and poleward energy transport. *Journal of Geophysical Research: Atmospheres*, *122*(20), 10578–10593. https://doi.org/10.1002/2017JD027221

Kramer, R. J., Matus, A. V., Soden, B. J., & L'Ecuyer, T. S. (2019). Observation-based radiative kernels from CloudSat/CALIPSO. *Journal of Geophysical Research: Atmospheres*, *124*(10), 5431–5444. https://doi.org/10.1029/2018JD029021

Pendergrass, A. G., Conley, A., & Vitt, F. M. (2018). Surface and top-of-atmosphere radiative feedback kernels for CESM-CAM5. *Earth System Science Data*, *10*(1), 317–324. https://doi.org/10.5194/essd-10-317-2018

Shell, K. M., Kiehl, J. T., & Shields, C. A. (2008). Using the radiative kernel technique to calculate climate feedbacks in NCAR's Community Atmospheric Model. *Journal of Climate*, *21*(10), 2269–2282. https://doi.org/10.1175/2007JCLI2044.1

Smith, C. J., Kramer, R. J., & Sima, A. (2020). The HadGEM3-GA7.1 radiative kernel: The importance of a well-resolved stratosphere. *Earth System Science Data*, *12*(3), 2157–2168. https://doi.org/10.5194/essd-12-2157-2020

Soden, B. J., Held, I. M., Colman, R., Shell, K. M., Kiehl, J. T., & Shields, C. A. (2008). Quantifying climate feedbacks using radiative kernels. *Journal of Climate*, *21*(14), 3504–3520. https://doi.org/10.1175/2007JCLI2110.1